ACS APPLIED ELECTRONIC MATERIALS

pubs.acs.org/acsaelm Article

Temperature-Stable $x(Na_{0.5}Bi_{0.5})MoO_4-(1-x)MoO_3$ Composite Ceramics with Ultralow Sintering Temperatures and Low Dielectric Loss for Dielectric Resonator Antenna Applications

Shu-Zhao Hao, Di Zhou,* Chao Du, Li-Xia Pang, Charanjeet Singh, Sergei Trukhanov, Alex Trukhanov, Antonio Sergio Bezerra Sombra, Jobin Varghese, Qiang Li, and Xiu-Qun Zhang

Cite This: *ACS Appl. Electron. Mater.* 2021, 3, 2286−2296 Read Online

ACCESS | Metrics & More | Article Recommendations | Supporting Information

ABSTRACT: Fifth-generation mobile communication systems provide a huge market for microwave dielectric materials, especially in the manufacture of dielectric resonators, filters, substrates, and antennas. Herein, an excellent performance microwave dielectric ceramic $x(NaBi)_{0.5}MoO_4-(1-x)MoO_3$ ($0.2 \le x \le 0.9$, abbreviated as xNBM−(1−x)MO sintered below 660 °C with two coexisting phases is prepared via a solid solution reaction. With the increasing x value, the sintering temperature rises from 600 to 640 °C. The dielectric properties have a series of changes with increasing permittivity (10.3−28.1), decreasing Q_f value (12,080 to 8600 GHz), and increasing τ_f value (−27.1 to +21.2 ppm/°C). Typically, at the ultralow temperature of 630 °C, the 0.8NBM−0.2MO ceramic exhibits great microwave performance with $\varepsilon_r \sim 24.4$, $Q_f \sim 9030$ GHz (7.7 GHz), and a near-zero $\tau_f \sim 7.2$ ppm/°C. A prototype dielectric resonator antenna is manufactured using a 0.8NBM−0.2MO ceramic. A high-impedance bandwidth ~360 MHz can be obtained in the antenna at 7.74 GHz with −10 dB transmission loss (S_{11}). Furthermore, the chemical compatibility with Al powder indicates that the xNBM−(1−x)MO composite ceramics may be promising microwave materials for applications in ultralow-temperature co-fired ceramic technology.

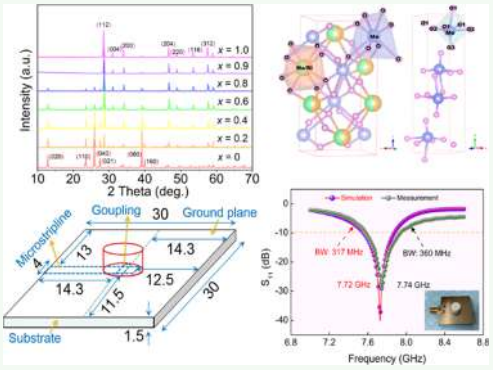

KEYWORDS: *ULTCC, molybdenum-based composite microwave ceramics, ultralow sintering temperature, Raman spectra, dielectric resonator antenna*

INTRODUCTION

The innovation of wireless communication technology drives the rapid development of related industries; especially, with the coming of fifth-generation wireless systems, the quantity demanded of microwave devices rapidly rises. Among them, the microwave dielectric antenna, applied in global positioning system navigation, mobile terminal, and communication stations, has received increasing attention from researchers.[1−3] Currently, the resources of the frequency band are steadily utilized, the millimeter wave band has become the researchers' main focus, and the DR dielectric resonator antennas (DRA) fabricated by the low loss microwave dielectric material makes a figure with its high radiant efficiency in the millimeter wave region. Meanwhile, the DRA has attractive features, such as small size, lightweight, and diversified mode of feeding, which are beneficial to the miniaturization and integrated design in microwave circuits. Hence, the microwave ceramic DRA will have a wide range of applications in the present and future mobile communications market.[4−6]

At present, massive MIMO (multiple input multiple output) is an effective means to enhance channel utilization for wireless communication.[7] Generally, it is expected that 64 or even 128 antennas will be used in this technology. Hence, a suitable fabrication method and antennas should be applied for large-scale integration. Low-temperature co-fired ceramic (LTCC) technology is an efficient working method to design and incorporate integrative microwave devices while providing technical support for the production of multiple-antenna MIMO systems. Meanwhile, the DR antennas have advantages for the miniaturization and integration in microwave circuits and are potential candidates for the application in MIMO systems. For LTCC technology, LTCCs are required to have low sintering temperature for cofiring with Ag electrodes (melting point ~961 °C), but classic microwave dielectric material has a high sintering temperature (>1000 °C); the research for the low sintering temperature microwave material has accelerated in recent years. To save energy and resources,

Received: February 28, 2021
Accepted: April 19, 2021
Published: May 4, 2021

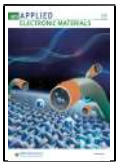

https://doi.org/10.1021/acsaelm.1c00193
ACS Appl. Electron. Mater. 2021, 3, 2286−2296

the so-called family of ultra-LTCC (ULTCC) technology comes up; the microwave ceramic applied in ULTCC technology should have a lower sintering temperature for cofiring with Al electrodes (melting point ~660 °C).[8−12] For DR antennas, the electromagnetic wave transmission happens inside the microwave ceramic, so there are some demands for the performance of microwave materials. First, a diverse permittivity (ε_r) can adjust the size of the dielectric material for the design requirements of the device. Second, high-quality factor ($Q = 1/\tan\delta$) brings the narrow passband and has the advantage to improve the transmission quality of the antenna. Finally, near-zero temperature coefficient of resonance frequency (τ_f) is an important parameter for the microwave device to stably work under different conditions.[13,14] Consequently, it is very important to find the microwave materials with low firing temperature, applicable permittivity, a high Q_f value, and a close to zero τ_f value for the application in LTCC technology and the manufacture of the DR antennas.

Recently, a mass of microwave materials prepared by the low melting temperature oxides, such as V_2O_5 (690 °C), TeO_2 (733 °C), and MoO_3 (790 °C), showed high-performance microwave dielectric properties and low-temperature sintering densification. Li et al. found that vanadium-base microwave ceramics $AgCa_2B_2V_3O_{12}$ (B = Mg, Zn) sintered below 740 °C display excellent dielectric properties (ε_r = 10.28 and 11.15, Q_f = 43,000 and 26,930 GHz, and τ_f = −69 and −95 ppm/°C).[15] Sebastian et al. reported a type of tellurium-base microwave material $Zn_2Te_3O_8$, which showed high microwave performance with $\varepsilon_r \sim 16.2$, $Q_f \sim 66{,}000$ GHz, and $\tau_f \sim -60$ ppm/°C, and the sintering temperature of this ceramic is below 700 °C.[16] However, tellurium oxide has a high price; Te-base and V-base compounds are chemical hazards that cause environmental problems. In comparison, Mo-based microwave materials are given serious attention by many researchers with its relatively low price and hypotoxicity. Varghese et al. reported that MoO_3 sintered at 650 °C has a ε_r = 6.6 and a Q_f = 41,000 GHz.[17] Then, Zhou et al. reported that the dielectric properties of the MoO_3 ceramic calcined at 660 °C have a ε_r = 7.6, a Q_f = 35,000 GHz, and τ_f = −39 ppm/°C.[18] Whereafter, the researchers discovered that the tetragonal scheelite ABO_4 microwave ceramics had flexible cation site occupancy to adjust microwave properties.[19,20] Zhou et al. reported the $(NaBi)_{0.5}MoO_4$ ceramic calcined at 690 °C with excellent microwave performances (ε_r = 34.4, Q_f = 12,300 GHz, and τ_f = +43 ppm/°C).[21] In our present work, a $Bi_{2/3}MoO_4$ ceramic was composited with a $(NaBi)_{0.5}MoO_4$ ceramic, and a near zero τ_f value (−13.7 ppm/°C) was obtained in the 0.8-$(NaBi)_{0.5}MoO_4$−0.2$Bi_{2/3}MoO_4$ ceramic with $\varepsilon_r \sim 29.8$ and Q_f ~11,800 GHz.[22] These compositions can be applied in LTCC technology and fabricated as a DR antenna.

Herein, the sintering behavior, phase analysis, microscopic structure, and microwave properties of the $x(NaBi)_{0.5}MoO_4$−$(1-x)MoO_3$ (xNBM−$(1-x)$MO, x = 0.2−0.9) composite ceramics are investigated. The metallic silver and aluminum were co-fired with the samples to find the chemical compatibility for these materials. Furthermore, the 0.8NBM−0.2MO ceramic is designed as a cylindrical antenna prototype using the $HE_{11\delta}$ fundamental pattern for slot excitation. The coefficient of reflectivity, radiation mode, and antenna dimension are simulated using commercial CST software. Then, based on the simulated design, the matching actual DRA was successfully manufactured.

EXPERIMENTAL SECTION

Sample Synthesis. High-purity oxides Bi_2O_3 (>99%), MoO_3 (>99.95%), and reagent grade carbonate Na_2CO_3 (>99%) were prepared for the synthesis of the $x(NaBi)_{0.5}MoO_4$−$(1-x)MoO_3$ (xNBM−$(1-x)$MO, x = 0.2−0.9) composite ceramics. The proportionate mixed powders were ball-milled for 4 h in alcohol. Next, the milled powders were dried at 100 °C in an oven for 1 h and calcined at 550 °C in a muffle furnace for 4 h. Then, the calcined powders were milled for 6 h again and dried for 12 h. Finally, the pretreatment powders were pressed into cylinders (10 mm diameter and 5 mm height) using an isostatic press at 250 MPa. The fashioned samples were sintered between 600 and 640 °C for 2 h.

Structural and Microstructural Characterizations. Room-temperature X-ray diffraction (XRD) was applied using Cu Kα radiation; the 2θ degree ranged from 10 to 70° at 0.02 step size. The surfaces of the samples and the microstructure of the co-fired ceramic with Al were studied using field-emission scanning electron microscopy (SEM) with energy-dispersive X-ray spectroscopy (EDS) analysis. For the measurement of Raman spectra, an Ar^+ laser (514.5 nm) pumping source was applied. IR reflectivity spectra were recorded using a Bruker Optik IFS 66v FTIR spectrometer (IFS 66v/S Vacuum; Bruker Optik GmbH, Germany). The chemical reactions of the raw materials were studied using differential scanning calorimetry (DSC) measurements and thermogravimetric analysis (NETZSCH-sta499C, Germany).

Microwave Dielectric Property and Antenna Measurement. The dielectric properties of the samples were measured with the $TE_{01\delta}$ shielded cavity method using a network analyzer (8720ES, Agilent, Palo Alto, CA) and a homemade heating system. The τ_f value was measured from 25 to 80 °C and calculated with the following formula

$$\tau_f = \frac{f_{85} - f_{25}}{f_{25}(85 - 25)} \times 10^6 \text{ ppm/°C} \quad (1)$$

where f_{85} and f_{25} represent the $TE_{01\delta}$ resonant frequency at 85 and 25 °C, respectively. Meanwhile, the transmission parameter S_{11} was tested using the same network analyzer. Design and simulation of the antenna were performed using CST software.

RESULTS AND DISCUSSION

Traditional phase diagrams show the equilibrium relationship between different phase states, such as a Na_2O−MoO_3 binary diagram[23] and a Bi_2O_3−MoO_3 binary diagram.[24] From these binary diagrams, it is easy to find the melting point of the complex compounds. Meanwhile, within the synthesis of the ceramic, the sintering temperature of the ceramic is related to the melting one; the phase diagram provides help for the prediction of the optimal sintering temperature of the ceramic. As shown in Figure 1, the different components of the xNBM−$(1-x)$MO composite ceramics (x = 0−1) were marked with a red circle in the Na_2O−Bi_2O_3−MoO_3 ternary phase diagram. According to the Na_2O−MoO_3 and Bi_2O_3−MoO_3 binary diagram, the melting points of the molybdenum base compounds focused largely on a 600−800 temperature interval; the sintering temperature of the xNBM−$(1-x)$MO ceramics (x = 0.2−0.9) should be estimated in this temperature range. According to Zhou's reports,[18,21] the optimal sintering temperature of the $(NaBi)_{0.5}MoO_4$ ceramic was 690 °C and the pure MoO_3 oxide sintered at 650 °C showed the best dielectric properties (ε_r = 7.6, Q_f = 35,000 GHz, and τ_f = −39 ppm/°C); the estimation of the sintering temperature was similar to these results.

In order to investigate the combination reaction and the thermal decomposition characteristics of the 0.8NBM−0.2MO composite dried powder during the sintering process, simultaneous thermal analysis (TG−DSC) and XRD are

https://doi.org/10.1021/acsaelm.1c00193
ACS Appl. Electron. Mater. 2021, 3, 2286−2296

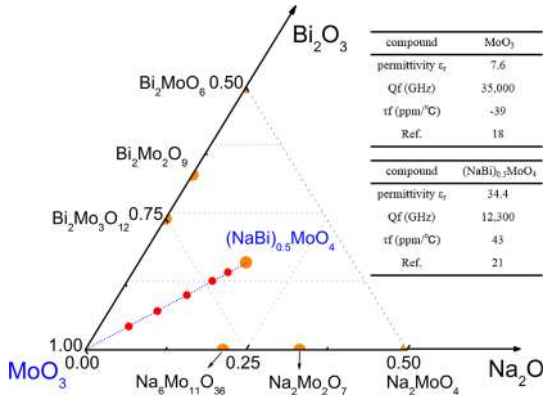

Figure 1. xNBM−(1−x)MO (x = 0.2−0.9) (red circle) ceramics in the Na_2O−Bi_2O_3−MoO_3 ternary phase diagram.

used. As shown in Figure 2a, based on the TG graph, the thermal decomposition can be divided into three steps. In the first step, a small weight loss value of about 1.95%, deriving from the evaporation of residual water, is obtained from ambient temperature to 110 °C. Meanwhile, a distinct endothermic peak can be observed in the DSC graph. In the second step between 110 °C and about 280 °C, the weight loss drops approximately 2%, and within the DSC analysis, an endothermic peak can be found near 270 °C; these results indicate that Na_2CO_3 reacted with MoO_3 and generated a new compound. Finally, when the temperature increases from 300 to 700 °C, the weight loss has slightly changed; the total weight loss value of approximately 4.7% is mainly from the evaporation of water and carbon dioxide generated from the chemical reaction. In the DSC curves, there are two endothermic peaks and one exothermic peak observed at around 500 °C; the likely reason is the decomposition of intermediate products and the synthesis of $(NaBi)_{0.5}MoO_4$ phase. Furthermore, the endothermic peak found at about 640 °C is derived from the melting of molybdenum base oxide. The XRD patterns of the 0.8NBM−0.2MO composite dried powder after thermal treatment at different temperatures are shown in Figure 2b. When the temperature is 270 °C, the dried powder is brown; the diffraction peaks of Bi_2O_3 and MoO_3 could be found in the XRD patterns; a new compound could be indexed as a $Na_6Mo_{10}O_{33}$ phase,[25] which has the chemical reaction

$$3Na_2CO_3 + 10MoO_3 \rightarrow Na_6Mo_{10}O_{33} + 3CO_2\uparrow \quad (2)$$

With the increase of temperature, the color of the powder turns yellow; the diffraction peak of the $Na_6Mo_{10}O_{33}$ phase enhances at 360 °C and weakens at 430 °C, and the $(NaBi)_{0.5}MoO_4$ phase appears at this moment. When the temperature heats up to 510 °C, the powder turns white, only the diffraction peaks of the $(NaBi)_{0.5}MoO_4$ phase and the MoO3 phase could be observed, and the $(NaBi)_{0.5}MoO_4$ phase has the following chemical reaction

$$Na_2O + Bi_2O_3 + 4MoO_3 \rightarrow 4NaBi_{0.5}MoO_4 \quad (3)$$

The room-temperature XRD patterns of the xNBM−(1−x)MO composite ceramics (x = 0.2−0.9) calcined at the optimal temperature are shown in Figure 2a. All diffraction peaks of the samples match well with the standard PDF card (no. 79-2240) and PDF card (no. 15-8256). The tetragonal phase structure of the $(NaBi)_{0.5}MoO_4$ ceramic and the monoclinic phase structure of the MoO_3 ceramic are observed in total components of the ceramics. As the x value increases, the intensities of (020), (110), (040), (021), and (060) peaks from the MoO_3 ceramic gradually decline, but the intensities of (112), (004), (200), (204), and (312) peaks from the $(NaBi)_{0.5}MoO_4$ ceramic enhance; this phenomenon is related to the proportion of the two different phases. However, only the diffraction peaks of the MoO_3 ceramic and $(NaBi)_{0.5}MoO_4$ ceramic could be seen in the XRD spectra. Hence, the synthesis of the xNBM−(1−x)MO composite ceramics is successful without any impurities. Moreover, the crystal structures of the MoO_3 ceramic and $(NaBi)_{0.5}MoO_4$ ceramic are shown in Figure 2b. In the MoO_3 monoclinic phase structure, there are three different oxygen atoms; the Mo atom connects with three O(1), two O(2), and one O(3) and composes a [MoO_6] octahedron.[26] In the $(NaBi)_{0.5}MoO_4$ tetragonal phase structure, the $(NaBi)^{4+}$ groups occupy the A-site, the Mo atom connects with four oxygen atoms and composes a [MoO_4] tetrahedron[27] (Figure 3).

As shown in Figure 4a−d, there are four SEM images recorded on the surfaces of the xNBM−(1−x)MO composite ceramics (x = 0.2−0.8). All samples are sintered at optimal temperature. When x is 0.2, the 0.2NBM−0.8MO ceramic presents two obvious phases with the claviform grains and small grains pack together. The grain size of the small one is about 1 μm and the height of the claviform one is about 7 μm. The sample presented a moderately dense microstructure.

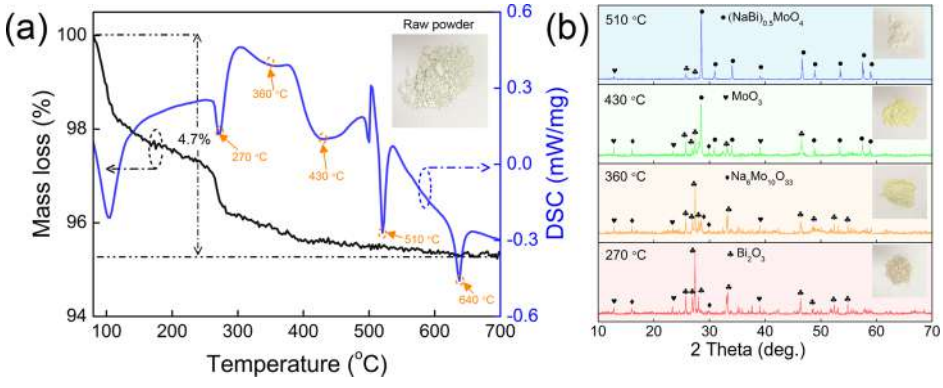

Figure 2. (a)TG-DSC graphs of the 0.8NBM−0.2MO composite dried powder, (b) XRD patterns of the 0.8NBM−0.2MO composite ceramic after thermal treatment at different temperatures (black clover Bi_2O_3, black diamond $Na_6Mo_{10}O_{33}$, black heartine MoO_3, black circle $(NaBi)0.5MoO_4$), with the inset figure exhibiting the calcined powders at different temperatures.

https://doi.org/10.1021/acsaelm.1c00193
ACS Appl. Electron. Mater. 2021, 3, 2286−2296

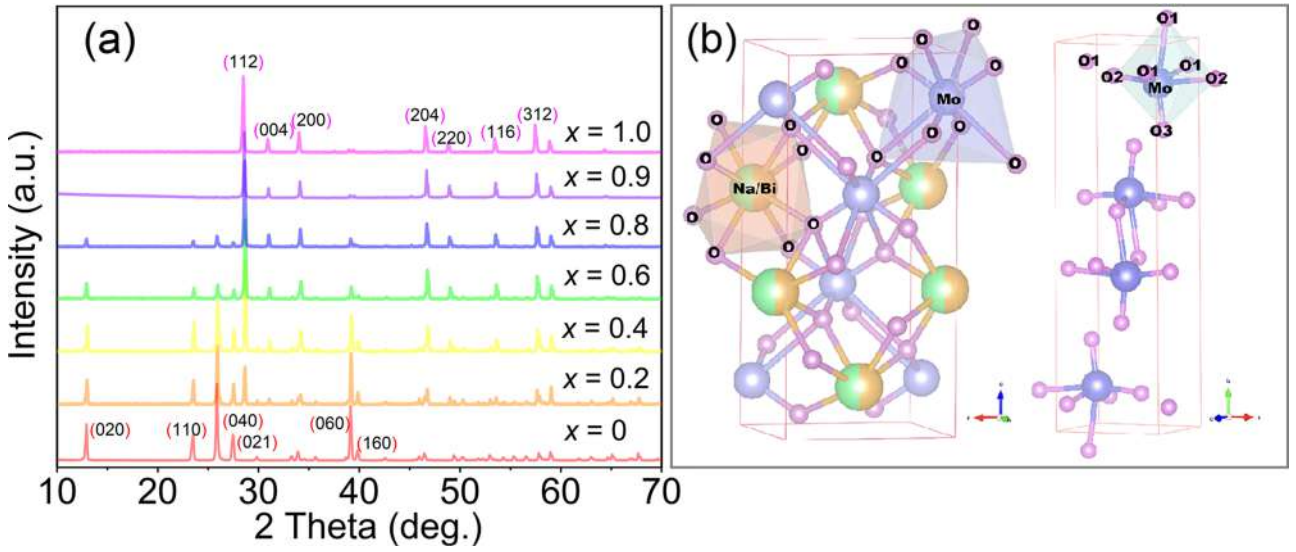

Figure 3. (a) XRD patterns of xNBM−(1−x)MO composite ceramics (x = 0−1). (b) Crystal structure of $(NaBi)0.5MoO_4$ phase and MoO_3 phase.

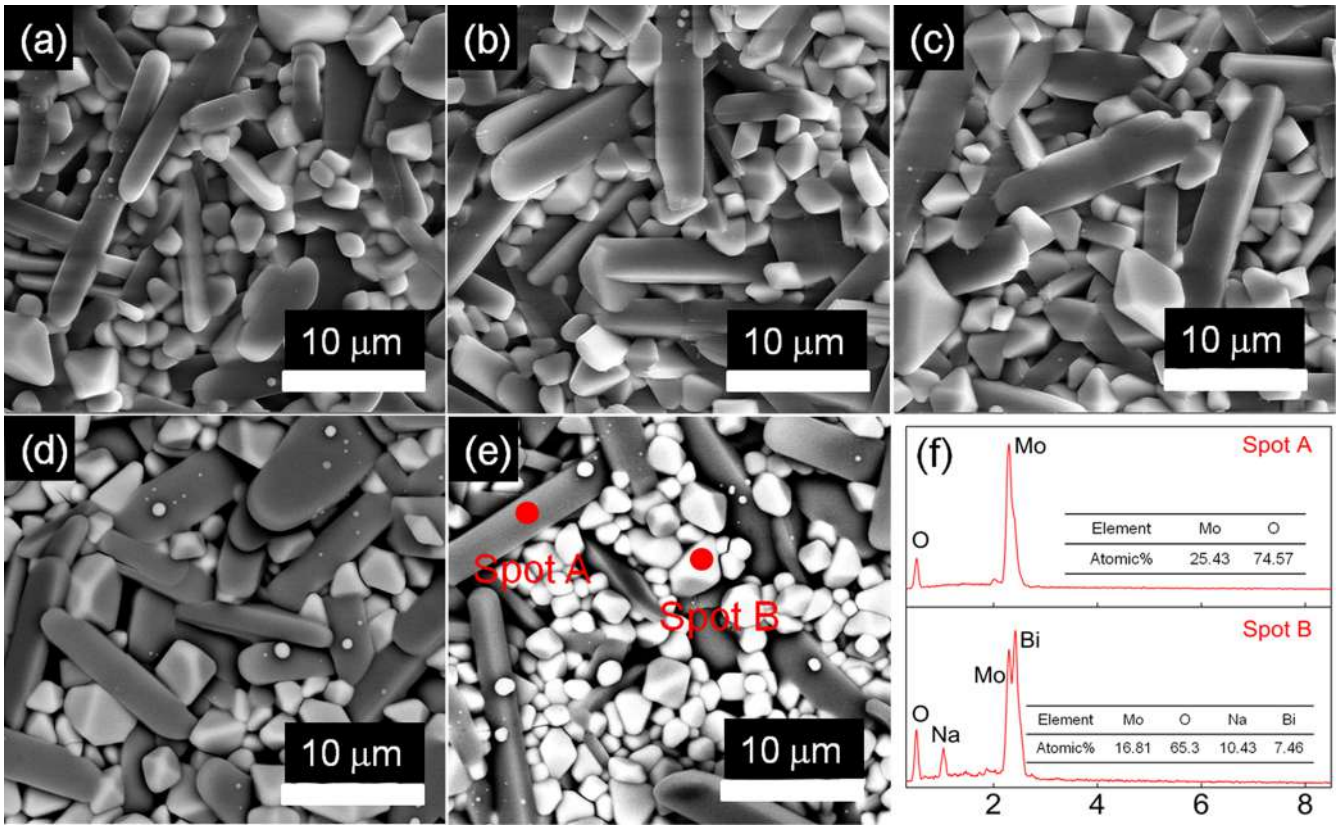

Figure 4. SEM images of surfaces of the xNBM−(1−x)MO composite ceramics sintered at different temperatures: (a) x = 0.2 (600 °C for 2 h), (b) x = 0.4 (610 °C for 2 h), (c) x = 0.6 (620 °C for 2 h), and (d) x = 0.8 (630 °C for 2 h). (e,f) BS-SEM image and EDS analysis of the 0.8NBM−0.2MO composite ceramic.

With the increasing x value, the sizes of two different grains all increase, which is probably due to the rising sintering temperature. To investigate the compounds of two different grains, backscattered electron image and EDS have been used. As shown in Figure 4e, the small grains present a light color and the claviform grains present a dark color in the 0.8NBM−0.2BMO ceramic. According to the EDS analysis in Figure 4f, the light color grains belong to the $(NaBi)_{0.5}MoO_4$ phase, while the dark color grains belong to the MoO_3 phase; the two different phases coexist in the 0.8NBM−0.2BMO ceramic. These results are consistent with the XRD analysis.

Raman spectrum is widely applied to investigate the phonon vibration characteristics of ceramics and is also used to identify the phase composition and study the order−disorder transitions and problems derived from the defects and impurities in ceramics. The xNBM−(1−x)MO composite ceramics have two phases with the tetragonal phase of the $(NaBi)_{0.5}MoO_4$ ceramic ($I4_{1/a}$ space group) and the

https://doi.org/10.1021/acsaelm.1c00193
ACS Appl. Electron. Mater. 2021, 3, 2286−2296

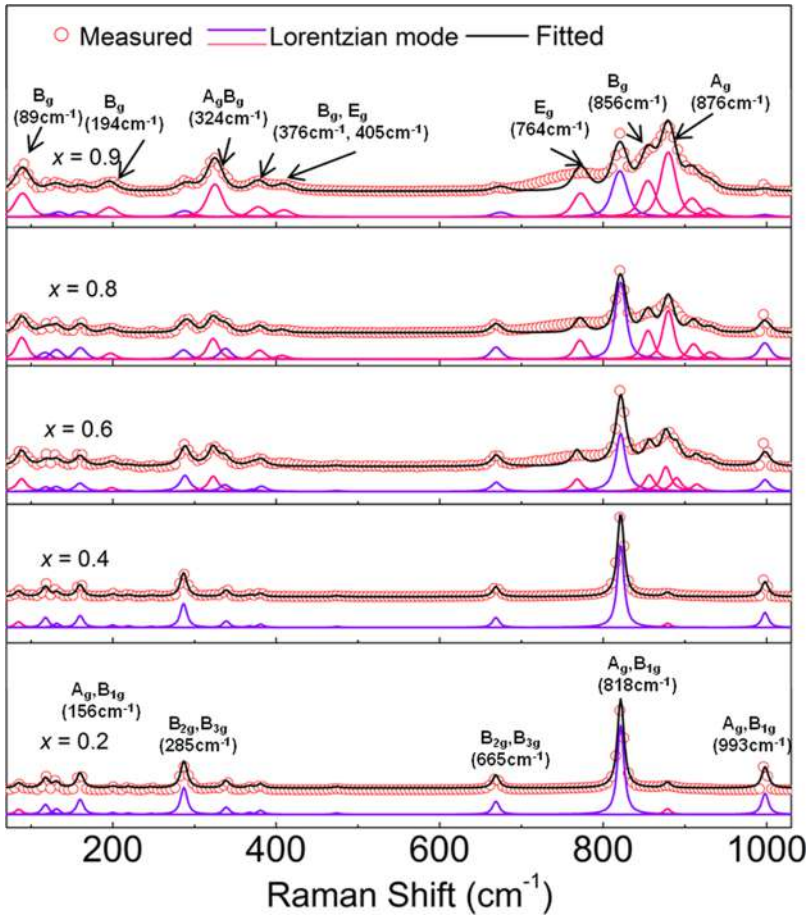

Figure 5. Measured and fitted Raman spectroscopy of the *x*NBM−(1−x)MO (*x* = 0.2−0.9) ceramics (purple lines MoO_3 and pink lines $(NaBi)0.5MoO_4$).

monoclinic phase of the MoO_3 ceramic (*Pbnm* space group). On the basis of the group theory, the $(NaBi)_{0.5}MoO_4$ ceramic has 26 vibration modes. The detailed parameters are shown as follows.

$$\Gamma = 3A_g + 5B_g + 5E_g + 5A_u + 3B_u + 5E_u \quad (4)$$

Among them, A_g, B_g, and E_g modes belong to Raman-active, while A_u and E_u modes belong to IR-active. Furthermore, as per Hanuza's report,[28] $2B_g$ and $2E_g$ Raman vibration modes can be subdivided into translational modes, A_g and E_g are divided into rotational modes, and the other Raman-active modes are related to the isolated MoO_4^{2-} ions. For the MoO_3 ceramic,[29] the complex vibration modes are shown as follows.

$$\Gamma = 8A_g + 8B_{1g} + 4B_{2g} + 4B_{3g} + 3A_u + 3B_{1u} + 6B_{2u} + 6B_{3u} \quad (5)$$

where A_g, B_{1g}, B_{2g}, and B_{3g} are Raman-active modes, while B_{1u}, B_{2u}, and B_{3u} are IR-active modes. As shown in Figure 5, when the *x* value is 0.2, there are nine obvious MoO_3 Raman-active modes located at 116 cm^{-1} (B_{2g}), 131 cm^{-1} (B_{3g}), 160 cm^{-1} (A_g, B_{1g}), 285 cm^{-1} (B_{2g}, B_{3g}), 339 cm^{-1} (A_g), 380 cm^{-1} (B_{1g}), 668 cm^{-1} (B_{2g}, B_{3g}), 822 cm^{-1} (A_g, B_{1g}), and 997 cm^{-1} (A_g, B_{1g}) and two $(NaBi)_{0.5}MoO_4$ Raman-active modes at 89 cm^{-1} (B_g) and 877 cm^{-1} (A_g). With the increase of *x*, the number of the vibrational modes of $(NaBi)_{0.5}MoO_4$ ceramic gradually goes up. Comparatively, considering the measurement precision and interaction between the Raman crystal modes, the number of vibrational modes of the MoO_3 ceramic decreases and the intensities of the peaks of the Raman-active modes dramatically weaken.

Among the MoO_3 Raman-active modes, the $A_g + B_{1g}$ band at 160 cm^{-1} is related to the translation of the rigid chains, the $B_{2g} + B_{3g}$ band at 285 cm^{-1} originates from the wagging mode of the doublet terminal oxygen atoms, the 668 cm^{-1} (B_{2g}, B_{3g}) band is derived from the simultaneous stretching and compressing of the Mo−O−Mo bridge along the *c* axis, the 822 cm^{-1} (A_g, B_{1g}) band is assigned to the symmetric stretching mode of the Mo═O bond, while that at 997 cm^{-1} (A_g, B_{1g}) is assigned to the asymmetric stretching mode of the Mo═O bond.[30,31] In the $(NaBi)_{0.5}MoO_4$ Raman-active modes, the 83 and 194 cm^{-1} B_g bands locate at the external phonon region, and the other bands locate at the internal phonon region. According to the previous research,[28,32] the 83 cm^{-1} band is associated with the translation pattern of the coupled Bi^{3+} and MoO_4^{2-}, while that at 194 cm^{-1} derives from the rotational movement of the coupled Na^+ and MoO_4^{2-}. The 324, 376, and 406 cm^{-1} (A_g, B_g, and E_g) bands are related to Mo−O bending vibrations, and 764, 856, and 876 cm^{-1} (A_g, B_g, and E_g) bands are related to the Mo−O stretching vibrations. With the increasing *x* value, the full width at half-maximum (fwhm) values of the MoO_3 Raman spectrum increase, indicating the crystallinity of the MoO_3 ceramic falloff. The basic data of the Lorentz model obtained by the fitting of Raman spectra of the *x*NBM−(1−*x*)MO ceramics are shown in Table 1. Meanwhile, the intensities of A_g (876 cm^{-1})

https://doi.org/10.1021/acsaelm.1c00193
ACS Appl. Electron. Mater. 2021, 3, 2286−2296

Table 1. Parameters of the Lorentz Model Obtained by the Fitting of Raman Spectra and Loss Values Calculated by Damping Equations of xNBM−(1−x)MO (x = 0.2−0.9) Ceramics

mode	B_g (Bi)		Bg (Na)		A_g, B_{1g} (Mo)		calculated
x	f (cm^{-1})	fwhm	f (cm^{-1})	fwhm	f (cm^{-1})	fwhm	tan σ (10^{-4})
0.2	83.76	8.53	199.67	7.12	159.44	7.29	9.55
0.4	84.34	8.72	199.71	9.06	159.48	7.41	10.49
0.6	88.31	16.45	199.66	12.77	159.74	7.56	14.78
0.8	89.34	18.18	196.51	19.07	159.79	8.07	21.52
0.9	89.36	18.88	194.41	26.91	159.55	10.81	27.85

and B_g (89, 194 cm^{-1}) increase, while the 324, 376, 764, and 856 cm^{-1} peaks appear, indicating that the $(NaBi)_{0.5}MoO_4$ phase gradually dominates the xNBM−(1−x)MO ceramics. However, the vibrational peaks from the MoO_3 ceramic can still be observed; there are two different phases coexisting in xNBM−(1−x)MO ceramics.

The measured permittivity ε_{meas} of xNBM−(1−x)MO (x = 0.2−0.9) composite ceramics is illustrated in Figure 6a. As the

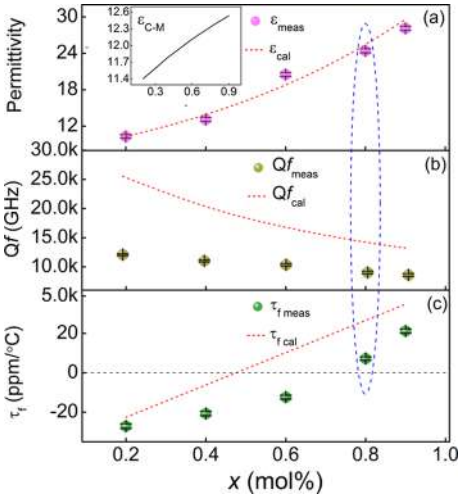

Figure 6. Microwave dielectric properties (permittivity, Q_f value, τ_f value) of the xNBM−(1−x)MO (x = 0.2−0.9) ceramics as a function of x.

$(NaBi)_{0.5}MoO_4$ composition increases from x = 0.2 to x = 0.9, the ε_{meas} value increases from 10.3 to 28.1. According to the previous reports, the permittivity of the $(NaBi)_{0.5}MoO_4$ ceramic (34.4) is larger than that of the MoO_3 ceramic (6.6) based on the Lichtenecker empirical logarithmic rule.[33]

$$\ln \varepsilon = v_1 \ln \varepsilon_1 + v_2 \ln \varepsilon_2 \quad (6)$$

where v_1 and ε_1 are the volume fraction and permittivity of the $(NaBi)_{0.5}MoO_4$ composition and v_2 and ε_2 are the volume fraction and permittivity of the MoO_3 composition. The volume fraction is reckoned using the following equation.[34]

$$v_x = \frac{m_x M_x/\rho_x}{\sum m_x M_X/\rho_X} \quad (7)$$

where x represents the $(NaBi)_{0.5}MoO_4$ and MoO_3 phases, m_x and M_x are the mole fraction and relative molecular mass of the different component, respectively, and ρ_x is the density of the different component. The calculated volume fractions of $(NaBi)_{0.5}MoO_4$ are 0.28, 0.51, 0.7, 0.86, and 0.93 for the mole fractions 0.2, 0.4, 0.6, 0.8, and 0.9, respectively. With the $(NaBi)_{0.5}MoO_4$ contents increasing, the calculated permittivity ε_{cal} also increases and remains the same change rule with the measured one. To further investigate the relationship between permittivity and polarizability, the Clausius−Mossotti (C−M) equation has been used.

$$\varepsilon_r = \frac{3V_m + 8\pi\alpha}{3V_m - 4\pi\alpha} \quad (8)$$

where V_m is the cell volume and α is the molecular polarizability; using the XRD data, the cell volume of the $(NaBi)_{0.5}MoO_4$ ceramic is 80.45 $Å^3$ (321.82/4), while that of the MoO_3 ceramic is 50.75 $Å^3$ (202.98/4). According to Shannon's additive rule,[35] polarizability mainly derives from the contribution of ionic and electronic components in the microwave region; total molecular polarizability of the complex compound should be estimated by summing the ionic polarizability of the total constituent ions. For the $(NaBi)_{0.5}MoO_4$ and MoO_3 phases, the molecular polarizability can be, respectively, described as follows

$$\alpha_{(NaBi)^{0.5}MoO^4} = 0.5\alpha_{Na^+} + 0.5\alpha_{Bi^{3+}} + \alpha_{Mo^{6+}} + 4\alpha_{O^{2-}} = 15.28\ Å^3 \quad (9)$$

$$\alpha_{MoO^3} = \alpha_{Mo^{6+}} + 3\alpha_{O^{2-}} = 9.31\ Å^3 \quad (10)$$

where the ionic polarizabilities of Na^+, Bi^{3+}, Mo^{6+}, and O^{2-} are 1.8, 6.12, 3.28, and 2.01 $Å^3$, respectively. Hence, the calculated permittivities of the $(NaBi)_{0.5}MoO_4$ and MoO_3 ceramics are 12.67 and 10.95, respectively. However, this additive rule is usually used to estimate the low permittivity materials; the calculated result of the $(NaBi)_{0.5}MoO_4$ ceramic is much smaller than the measured one. Based on eq 5, the $\varepsilon_{C\text{-}M}$ value can be obtained. As shown in the inset of Figure 6, the calculated permittivity $\varepsilon_{C\text{-}M}$ increases as a function of x, and the result is similar to the variation trend of the measured permittivity. Furthermore, the IR spectra are used to further investigate the complex dielectric response of the xNBM−(1−x)MO (x = 0.2−0.9) composite ceramics. When the x value is 0.8, the measured and fitted IR spectra of the 0.8NBM−0.2MO ceramic are shown in Figure S1; the fitted data indicate that the dielectric polarization of this composite ceramic was mainly dominated by the electronic and ionic polarization.

As shown in Figure 6b, the relationship between the Q_f value and the content of the $(NaBi)_{0.5}MoO_4$ ceramic can be observed. With the increase of x, the measured quality factor value Q_{meas} decreases from 12,080 to 8600 GHz. Based on the previous reports,[18,21] the quality factor of the MoO_3 ceramic (35,000 GHz) is larger than that of the $(NaBi)_{0.5}MoO_4$ ceramic (12,300 GHz); the Q_f value of the xNBM−(1−x)MO ceramics can be calculated using the following mixture rule.[36]

$$Q^{-1} = v_1 Q_1^{-1} + v_2 Q_2^{-1} \quad (11)$$

https://doi.org/10.1021/acsaelm.1c00193
ACS Appl. Electron. Mater. 2021, 3, 2286−2296

Table 2. Some Typical Low-Temperature Composite Ceramics and Their Properties

ceramics	S.T. (°C)	ε_r	Q_f (GHz)	τ_f (ppm/°C)	references
$0.12NaCa_4V_5O_{17}-0.88BaV_2O_6$	550	10.9	15,500	−1	42
8 wt % $Li_2CO_3+Ba_3V_2O_8$	660	13.1	33,000	13	43
$0.25Na_2Mo_2O_7-0.75Na_{0.5}Bi_{0.5}MoO_4$	580	24	13,000	3	44
$0.2MoO_3-0.8Na_{0.5}Bi_{0.5}MoO_4$	630	24.4	9030	7.2	this work
$BaTe_4O_9$ + 40 wt % $TiTe_3O_8$	575	25	19,300	−3	45
$0.47BaTe_4O_9-0.53TiTe_3O_8$	560	28	12,000	4	46

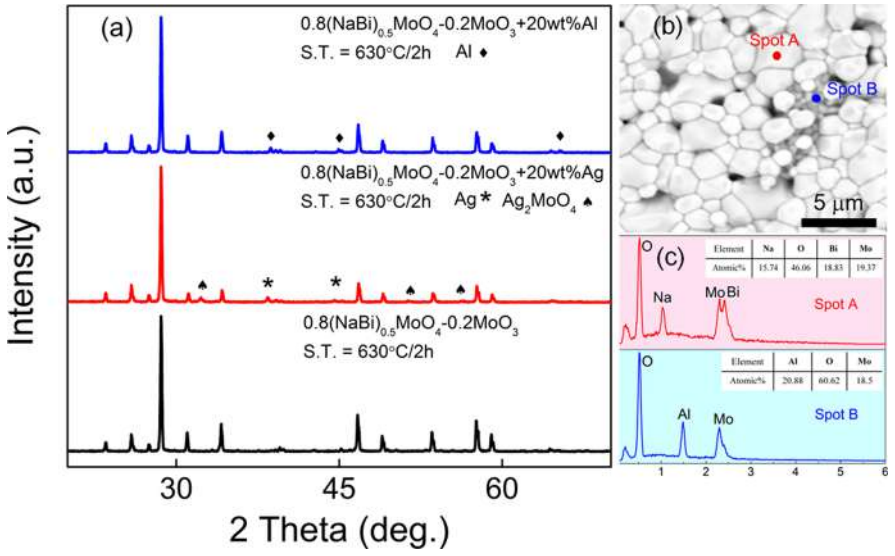

Figure 7. (a) XRD patterns of the 0.8NBM−0.2MO ceramic co-fired with 20 wt % Al and Ag powders sintered at 630 °C for 2 h. (b) Back-scattered electron image of the 0.8NBM−0.2MO ceramic co-fired with 20 wt % Al powders at 630 °C and (c) EDS analysis of the 0.8NBM−0.2MO ceramic co-fired with 20 wt % Al powders at 630 °C.

where Q, Q_1, and Q_2 are the Q_f values of the xNBM−(1−x)MO (x = 0.2−0.9) ceramics, $(NaBi)_{0.5}MoO_4$ ceramic, and MoO_3 ceramic, respectively. The volume fractions of the $(NaBi)_{0.5}MoO_4$ ceramic and MoO_3 ceramic are represented as v_1 and v_2, respectively. The calculated quality factor value Q_{cal} also decreases with increasing x, but the Q_{cal} value is significantly larger than the Q_{meas} one. The dielectric loss of microwave materials contains two categories with an intrinsic part and an external part; the intrinsic part is mainly controlled by the lattice vibration mode, and the external part is mainly influenced by the joint action of the second phase, defects, and the compactness. For the composite ceramics, the compactness of the sample is lower than that of the single phase; especially the MoO_3 ceramic cannot be well densified using the solid-state method. Furthermore, on the basis of the DSC result, when the sintering temperature is above 640 °C, the MoO_3 phase would fuse, while the grain of the $(NaBi)_{0.5}MoO_4$ phase could not grow well. As the x value increases, the grain size of the composite ceramic is smaller than that of the independent $(NaBi)_{0.5}MoO_4$ ceramic, which leads to the increase of the grain boundaries and pores and the decrease of Q_f values.

Moreover, to further study the variation of the dielectric loss, the damping equation can be used. Meanwhile, the fwhm values of the Raman spectra are closely related to the damping factor. Hence, according to the classical radiation theory, the dielectric loss can be calculated using the following equations.[37]

$$\text{fwhm} = \frac{\gamma\sqrt{\gamma^2 + 4\omega^2}}{2\omega} \tag{12}$$

$$\tan\sigma = \left(\frac{\gamma}{\omega_T^{\,2}}\right)\omega \tag{13}$$

where the damping factor is defined as γ, ω is the central frequency of the B_g mode at the external phonon region, and ω_T is the angular frequency of the transverse optical mode. In general, intrinsic dielectric loss is inversely proportional to the Q_f value. In this work, the dielectric loss value of the composite ceramic is calculated using the mixture rule, and the calculated data are exhibited in Table 1. As the x value varies from 0.2 to 0.9, the dielectric losses increase from 9.55×10^{-4} to 27.85×10^{-4}. Hence, the Q_f values of the xNBM−(1−x)MO ceramics decrease with the increase in x value.

The τ_f value of the xNBM−(1−x)MO (x = 0.2−0.9) composite ceramics can be observed in Figure 8c. According to the Lichtenecker logarithmic rule,[38] the calculated τ_f value can be obtained using the following equation.

$$\tau_f = v_1\tau_{f1} + v_2\tau_{f2} \tag{14}$$

where τ_{f1} and τ_{f2} are the τ_f values of $(NaBi)_{0.5}MoO_4$ and MoO_3, respectively. In Figure 8c, as the x value increases from 0.2 to 0.9, the measured and the calculated temperature coefficients all increase because the positive τ_f of $(NaBi)_{0.5}MoO_4$ (+43 ppm/°C) can compensate the negative τ_f of MoO_3 (−39 ppm/°C). When the x value is 0.8, a near-zero τ_f value (+7.2 ppm/°C) can be obtained, and the 0.8NBM−0.2MO ceramic sintered at 630 °C shows good dielectric performance (ε_r = 24.4 and Q_f = 9030 GHz). The other state-of-the-art materials are shown in Table 2 these microwave materials have good performance and prospects of application

https://doi.org/10.1021/acsaelm.1c00193
ACS Appl. Electron. Mater. 2021, 3, 2286−2296

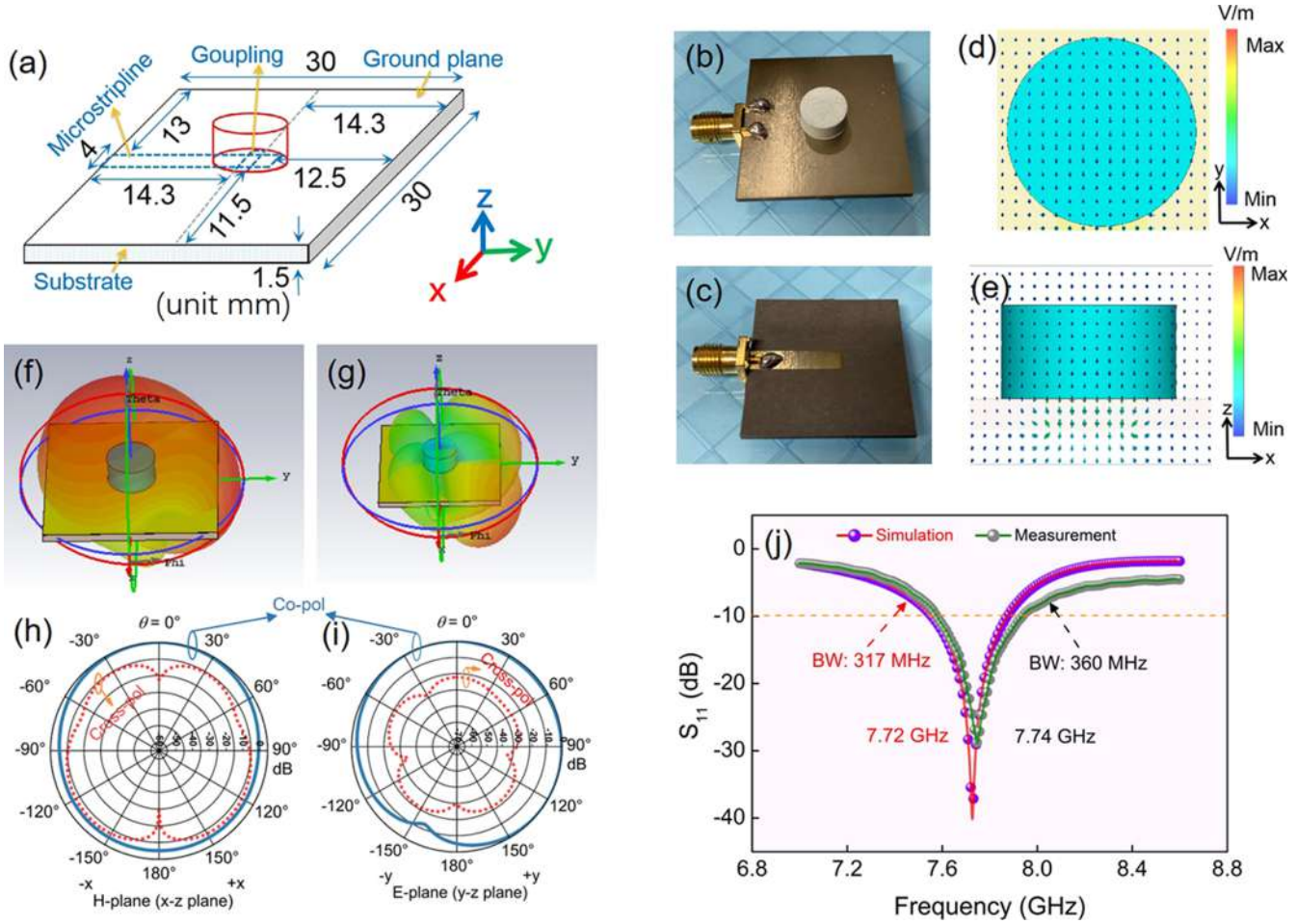

Figure 8. (a) Diagrams of the geometry configuration for the designed slot-coupled DRA (unit: mm), the size dimension of the proposed cylindrical 0.8NBM−0.2MO ceramic DRA are d = 7.94 mm, h = 4.25 mm. (b) Top view and (c) bottom view of the manufactured DRA. Distributions of the (d) electric (*xoy* plane) and (e) magnetic (*xoz* plane) field for the slot-coupled DRA at 7.72 GHz. The simulation 3D radiation pattern of the (f) co-polarized and (g) cross-polarized for the antenna at 7.72 GHz. Simulated radiation patterns of the prototype in the (h) *xoz* plane and (i) *yoz* plane. (j) Simulated (purple curve) and measured (green curve) reflection coefficient of the slot-coupled DRA as a function of frequency.

in LTCC technology. Hence, the 0.8NBM−0.2MO ceramic has good potential as a low-temperature microwave ceramic in the LTCC or ULTCC technology.

As we know, there are two key points for the application of the microwave ceramic in LTCC or ULTCC technology. One is that the microwave ceramic should have a low sintering temperature for co-firing with the metal electrode; the other is that the microwave ceramic should have good chemical compatibility with the electrode material. In this work, the sintering temperature of the 0.8NBM−0.2MO ceramic is 630 °C, which is lower than the melting point of silver (~961 °C) and aluminum (~660 °C); this ceramic has the possibility to be used in LTCC or ULTCC technology. Furthermore, to evaluate the chemical compatibility of the 0.8NBM−0.2MO ceramic with silver and aluminum electrodes, it was co-fired with 20 wt % Ag and Al powders at 630 °C for 2 h. Figure 7a shows the XRD patterns of the co-fired ceramic. From the XRD results, it is clearly observed that the silver powders react with the 0.8NBM−0.2MO ceramic to form the Ag_2MoO_4 phase, but the aluminum powders do not react with the 0.8NBM−0.2MO ceramic and only the diffraction peaks of 0.8NBM−0.2MO and Al were detected. Moreover, it can be clearly seen in Figure 7b that there are two different grains in the back-scattered electron image; the large one with a light color (marked as A) and the small ones with a dark color (marked as B). EDS analysis is used to identify the chemical components of the two different color grains, and the measured results are shown in Figure 7c. Based on these results, the large grains should be the $(NaBi)_{0.5}MoO_4$ phase, whereas the small grains should be the concentration area of the MoO_3 and Al phases. The results indicate that the 0.8NBM−0.2MO ceramic has good chemical compatibility with an aluminum electrode, although it reacts with a silver electrode. Compared with silver used in the LTCC technology, aluminum can be employed as a cheaper electrode material for the ULTCC technology. Hence, all of the above results imply that the 0.8NBM−0.2MO ceramic could be a possibility for applications in ULTCC multilayer microwave devices.

Antennas applied as the important components of the wireless apparatus have drawn much attention, especially in the rapid development of the wireless fifth-generation (5G) communication system. Among them, the dielectric resonator antennas (DRA) have gained a competitive advantage with their attractive characteristics of diversified shape, small size, lightweight, high operating-frequency bandwidth, and easy excitation. Generally speaking, the microwave dielectric

https://doi.org/10.1021/acsaelm.1c00193
ACS Appl. Electron. Mater. 2021, 3, 2286−2296

materials with low losses can be produced as DRAs.[39,40] The 0.8NBM−0.2MO ceramic has low losses and good temperature stability (near-zero τ_f value means that the ceramic has good temperature stability) and can be used for DRA as a promising material. To prove its possibility, a cylindrical 0.8NBM−0.2MO ceramic sample was designed as a slot-coupled DR antenna with a microstrip slot feed structure using the commercial CST Microwave Studio simulation software. As shown in Figure 8a, the geometry configuration of the designed DRA can be observed. In this diagram, the device has two components: one is the cylindrical 0.8NBM−0.2MO ceramic disc DR with 7.94 mm diameter and 4.25 mm height and the other is a square Rogers RT5880 substrate with 30 mm side length and 1.5 mm thickness. The center of the earthed substrate etches a slot, and the bottom of the DR is fixed on it. Based on the above design, it is anticipated that broadside radiation modes can be obtained in the DR, resonating at the fundamental mode $HE_{11\delta}$, and the DRA serves as a radiator and can be excited by the slot with a similar mode to $HE_{11\delta}$. As shown in Figure 8b,c, the prototype is manufactured according to the simulation design. Then, the distributions of electric and magnetic fields at 7.72 GHz are studied to expose the physical mechanism of the custom-designed DRA. Figure 8d shows the simulated electric field on the top of the DRA. The current displacement is along the negative *y*-axis direction in this designed DRA.[41] Figure 8e shows the simulated distribution of the magnetic field in this designed DRA. The radiation presents an elliptical pattern on the *yoz* plane, which is related to the oscillating movement of the electromagnetic waves between the internal planet and the microstrip line along the *z*-axis. These two figures indicate that the cylindrical 0.8NBM−0.2MO ceramic DR $HE_{11\delta}$ mode is excited. The simulated radiation modes of the designed DRA are shown in Figure 8f−i. For the *xoz* plane (*H*-plane) mode in the boresight direction ($\theta = 0°$), the cross-polarization fields are weaker than the co-polarization fields, and the transmission loss exceeds 20 dB. This result is similar to the *yoz* plane (*E*-plane) mode. The simulated and measured reflection coefficients of the cylindrical DRA are shown in Figure 8j. The simulated center frequency and the measured one are 7.72 and 7.74 GHz, while the simulated bandwidth and the measured one are 317 and 360 MHz ($S_{11} < -10$ dB), respectively. Therefore, the simulated center frequency matches well with the experimental data, and the simulated bandwidth is close to the experimental result.

CONCLUSIONS

In summary, the xNBM−$(1-x)$MO composite ceramics (x = 0.2−0.9) are successfully prepared via a solid solution reaction. The sintering behavior, microstructure, and microwave dielectric properties have been investigated systematically in this work. According to the XRD and Raman analysis, the measured results indicate that the monoclinic MoO_3 phase and tetragonal $(NaBi)_{0.5}MoO_4$ phase coexist with each other in the xNBM−$(1-x)$MO composite ceramics. Based on the measurement data of the microwave dielectric properties, the permittivity of the xNBM−$(1-x)$MO composite ceramics increases with the addition of the $(NaBi)_{0.5}MoO_4$ component, the quality factor decreases, while the τ_f value increases from −27.1 to +21.2 ppm/°C. Furthermore, the best dielectric properties of $\varepsilon_r \sim 24.4$, $Q_f \sim 9030$ GHz, and a near-zero $\tau_f \sim$ 7.2 ppm/°C are obtained for the 0.8NBM−0.2MO samples with the sintering temperature of 630 °C. The prototype DRA manufactured with the 0.8NBM−0.2MO ceramic exhibits a good performance with a bandwidth ∼360 MHz ($S_{11} < -10$ dB) at 7.74 GHz. The cofiring studies indicate that Ag powder reacts with the 0.8NBM−0.2MO ceramic, but Al powder has good chemical compatibility with this ceramic. Hence, ultralow temperature sintered xNBM−$(1-x)$MO composite ceramics are hopeful to be potential candidates for ULTCC applications, and the 0.8NBM−0.2MO ceramic is promising to be used in the 5G field due to its low loss and temperature stability characteristics.

ASSOCIATED CONTENT

Supporting Information

The Supporting Information is available free of charge at https://pubs.acs.org/doi/10.1021/acsaelm.1c00193.

Infrared reflectivity spectra, measured and calculated permittivity $\varepsilon'(\omega)$, measured and calculated dielectric loss $\varepsilon''(\omega)$ of the 0.8NBM−0.2MO ceramic, and values of parameters derived from the fitting of the IR spectra of the 0.8NBM−0.2MO ceramic (PDF)

AUTHOR INFORMATION

Corresponding Author

Di Zhou − *Key Laboratory of Multifunctional Materials and Structures, Ministry of Education, School of Electronic Science and Engineering, Xi'an Jiaotong University, Xi'an, Shaanxi 710049, China;* orcid.org/0000-0001-7411-4658; Email: zhoudi1220@gmail.com

Authors

Shu-Zhao Hao − *Key Laboratory of Multifunctional Materials and Structures, Ministry of Education, School of Electronic Science and Engineering, Xi'an Jiaotong University, Xi'an, Shaanxi 710049, China*

Chao Du − *Key Laboratory of Multifunctional Materials and Structures, Ministry of Education, School of Electronic Science and Engineering, Xi'an Jiaotong University, Xi'an, Shaanxi 710049, China*

Li-Xia Pang − *Micro-optoelectronic Systems Laboratories, Xi'an Technological University, Xi'an, Shaanxi 710032, China*

Charanjeet Singh − *School of Electronics and Communication Engineering, Lovely Professional University, Jalandhar, Punjab 144411, India*

Sergei Trukhanov − *National University of Science and Technology "MISiS", Moscow 4119049, Russia; South Ural State University, Chelyabinsk 454080, Russia; Scientific and Practical Materials Research Center of the NAS of Belarus, Minsk 220072, Belarus*

Alex Trukhanov − *National University of Science and Technology "MISiS", Moscow 4119049, Russia; South Ural State University, Chelyabinsk 454080, Russia; Scientific and Practical Materials Research Center of the NAS of Belarus, Minsk 220072, Belarus;* orcid.org/0000-0003-3430-9578

Antonio Sergio Bezerra Sombra − *Telecommunication Engineering Department, Telecommunication and Materials Science and Engineering of Laboratory (LOCEM), Physics Department, Federal University of Ceará (UFC), Fortaleza, Ceará 60455-760, Brazil*

https://doi.org/10.1021/acsaelm.1c00193
ACS Appl. Electron. Mater. 2021, 3, 2286−2296

Jobin Varghese − *Jobin Hybrid Microsystems, Fraunhofer Institute for Ceramic Technology and Systems IKTS, Dresden 01277, Germany;* orcid.org/0000-0003-3985-9181
Qiang Li − *ZTE Corporation, Shenzhen 518000, China*
Xiu-Qun Zhang − *ZTE Corporation, Nanjing 210012, China*

Complete contact information is available at: https://pubs.acs.org/10.1021/acsaelm.1c00193

Notes

The authors declare no competing financial interest.

■ ACKNOWLEDGMENTS

This work was supported by the National Key Research and Development Program of China (grant 2017YFB0406301), the National Natural Science Foundation of China (51972260, 52072295), the Fundamental Research Funds for the Central University (nos. xzy022020046), the 111 Project of China (B14040), and Open Funding of State Key Laboratory of Advanced Materials and Electronic Components (FHR-JS-202011003). The authors thank the administrators at the IR beamline workstation (BL01B) of National Synchrotron Radiation Laboratory (NSRL) for their help in the IR measurement and fitting. The SEM were done at the International Center for Dielectric Research (ICDR), Xi′an Jiaotong University, Xi′an, China, and the authors thank Ms. Yan-Zhu Dai for the help in using SEM.

■ REFERENCES

(1) Krishna, M. B.; Lloret Mauri, J. *Advances in Mobile Computing and Communications: Perspectives and Emerging Trends in 5G Networks*; CRC Press: Boca Raton, 2016.
(2) Lim, E. H.; Leung, K. W. Transparent dielectric resonator antennas for optical applications. *IEEE Trans. Antenn. Propag.* **2010**, *58*, 1054−1059.
(3) Wenmei, Z.; Xinwei, C. Overview of co-design approach to RF filter and antenna. *ZTE Commun.* **2020**, *16*, 61−66.
(4) Xiao, K.; Gong, L.; Kadoch, M. Opportunistic multicast NOMA with security concerns in a 5G massive MIMO system. *IEEE Commun. Mag.* **2018**, *56*, 91−95.
(5) Leung, K. W.; Fang, X. S.; Pan, Y. M.; Lim, E. H.; Luk, K. M.; Chan, H. P. Dual-function radiating glass for antennas and light covers—Part II: Dual-band glass dielectric resonator antennas. *IEEE Trans. Antenn. Propag.* **2013**, *61*, 587−597.
(6) Leung, K. W.; Pan, Y. M.; Fang, X. S.; Lim, E. H.; Luk, K.-M.; Chan, H. P. Dual-function radiating glass for antennas and light covers—Part I: Omnidirectional glass dielectric resonator antennas. *IEEE Trans. Antenn. Propag.* **2013**, *61*, 578−586.
(7) Larsson, E. G.; Edfors, O.; Tufvesson, F.; Marzetta, T. L. Massive MIMO for next generation wireless systems. *IEEE commun. Mag* **2014**, *52*, 186−195.
(8) Sebastian, M. T.; Jantunen, H. Low loss dielectric materials for LTCC applications: a review. *Int. Mater. Rev.* **2008**, *53*, 57−90.
(9) Sebastian, M. T.; Wang, H.; Jantunen, H. Low temperature co-fired ceramics with ultra-low sintering temperature: a review. *Curr. Opin. Solid State Mater. Sci.* **2016**, *20*, 151−170.
(10) Guo, H.-H.; Zhou, D.; Pang, L.-X.; Qi, Z.-M. Microwave dielectric properties of low firing temperature stable scheelite structured (Ca, Bi)(Mo, V)O_4 solid solution ceramics for LTCC applications. *J. Eur. Ceram. Soc.* **2019**, *39*, 2365−2373.
(11) Joseph, N.; Varghese, J.; Teirikangas, M.; Vahera, T.; Jantunen, H. Ultra-low-temperature cofired ceramic substrates with low residual carbon for next-generation microwave applications. *ACS Appl. Mater. Interfaces* **2019**, *11*, 23798−23807.
(12) Varghese, J.; Siponkoski, T.; Sobocinski, M.; Vahera, T.; Jantunen, H. Multilayer functional tapes cofired at 450 °C: Beyond HTCC and LTCC Technologies. *ACS Appl. Mater. Interfaces* **2018**, *10*, 11048−11055.
(13) Guo, H.-H.; Fu, M.-S.; Zhou, D.; Du, C.; Wang, P.-J.; Pang, L.-X.; Liu, W.-F.; Sombra, A. S. B.; Su, J.-Z. Design of a High-Efficiency and-Gain Antenna Using Novel Low-Loss, Temperature-Stable $Li_2Ti_{1-x}(Cu_{1/3}Nb_{2/3})_xO_3$ Microwave Dielectric Ceramics. *ACS Appl. Mater. Interfaces* **2021**, *13*, 912−923.
(14) Du, C.; Guo, H.-H.; Zhou, D.; Chen, H.-T.; Zhang, J.; Liu, W.-F.; Su, J.-Z.; Liu, H.-W. Dielectric resonator antennas based on high quality factor $MgAl_2O_4$ transparent dielectric ceramics. *J. Mater. Chem. C* **2020**, *8*, 14880−14885.
(15) Chen, J.; Tang, Y.; Xiang, H.; Fang, L.; Porwal, H.; Li, C. Microwave dielectric properties and infrared reflectivity spectra analysis of two novel low-firing $AgCa_2B_2V_3O_{12}$ (B = Mg, Zn) ceramics with garnet structure. *J. Eur. Ceram. Soc.* **2018**, *38*, 4670−4676.
(16) Subodh, G.; Sebastian, M. T. Glass-free $Zn_2Te_3O_8$ microwave ceramic for LTCC applications. *J. Am. Ceram. Soc.* **2007**, *90*, 2266−2268.
(17) Varghese, J.; Siponkoski, T.; Nelo, M.; Sebastian, M. T.; Jantunen, H. Microwave dielectric properties of low-temperature sinterable α-MoO_3. *J. Eur. Ceram. Soc.* **2018**, *38*, 1541−1547.
(18) Zhou, D.; Pang, L.-X.; Wang, D.-W.; Reaney, I. M. Novel water-assisting low firing MoO_3 microwave dielectric ceramics. *J. Eur. Ceram. Soc.* **2019**, *39*, 2374−2378.
(19) Kim, E. S.; Jeon, C. J.; Clem, P. G. Effects of crystal structure on the microwave dielectric properties of ABO_4 (A= Ni, Mg, Zn and B= Mo, W) ceramics. *J. Am. Ceram. Soc.* **2012**, *95*, 2934−2938.
(20) Zhou, D.; Pang, L.-X.; Guo, J.; Zhang, G.-Q.; Wu, Y.; Wang, H.; Yao, X. Low temperature firing microwave dielectric ceramics $(K_{0.5}Ln_{0.5})MoO_4$ (Ln = Nd and Sm) with low dielectric loss. *J. Eur. Ceram. Soc.* **2011**, *31*, 2749−2752.
(21) Zhou, D.; Randall, C. A.; Pang, L.-X.; Wang, H.; Guo, J.; Zhang, G.-Q.; Wu, Y.; Guo, K.-T.; Shui, L.; Yao, X. Microwave dielectric properties of $(ABi)_{1/2}MoO_4$ (A= Li, Na, K, Rb, Ag) type ceramics with ultra-low firing temperatures Mate. *Chem. Phys.* **2011**, *129*, 688−692.
(22) Hao, S.-Z.; Zhou, D.; Hussain, F.; Liu, W.-F.; Su, J.-Z.; Wang, D.-W.; Wang, Q.-P.; Qi, Z.-M.; Singh, C.; Trukhanov, S. Structure, spectral analysis and microwave dielectric properties of novel $x(NaBi)_{0.5}MoO_4$-$(1-x)Bi_{2/3}MoO_4$ (x = 0.2 ∼ 0.8) ceramics with low sintering temperatures. *J. Eur. Ceram. Soc.* **2020**, *40*, 3569−3576.
(23) Caillet, P. Anhydrous sodium or potassium polymolybdates and polytungstates. *Bull. Soc. Chim. Fr.* **1967**, *12*, 4750−4755.
(24) Chen, T.; Smith, G. S. The compounds and the phase diagram of MoO_3-Rich Bi_2O_3-MoO_3 system. *J. Solid State Chem.* **1975**, *13*, 288−297.
(25) Gatehouse, B. M.; Jenkins, C. E.; Miskin, B. K. The crystal structure of a sodium molybdenum oxide, $Na_6Mo_{10}O_{33}$, containing cross-linked chains of octahedra and square pyramids. *J. Solid State Chem.* **1983**, *46*, 269−274.
(26) Chithambararaj, A.; Yogamalar, N. R.; Bose, A. C. Hydrothermally Synthesized h-MoO_3 and α-MoO_3 Nanocrystals: New Findings on Crystal-Structure-Dependent Charge. *Transport. Cryst. Growth Des.* **2016**, *16*, 1984−1995.
(27) Kato, H.; Matsudo, N.; Kudo, A. Photophysical and photocatalytic properties of molybdates and tungstates with a scheelite structure. *Chem. Lett.* **2004**, *33*, 1216−1217.
(28) Hanuza, J.; Mączka, M.; Macalik, L.; van der Maas, J. Polarized Raman spectra of NaBi $(MoO_4)_2$ crystal and order—disorder effect in solid scheelites. *J. Mol. Struct.* **1994**, *325*, 119−124.
(29) Beattie, I. R.; Gilson, T. R. Single crystal laser Raman spectroscopy. *Proc. R. Soc. London, Ser. A* **1968**, *307*, 407−429.
(30) Gershinsky, G.; Yoo, H. D.; Gofer, Y.; Aurbach, D. Electrochemical and spectroscopic analysis of Mg^{2+} intercalation into thin film electrodes of layered oxides: V_2O_5 and MoO_3. *Langmuir* **2013**, *29*, 10964−10972.

(31) Mestl, G.; Ruiz, P.; Delmon, B.; Knozinger, H. Oxygen-exchange properties of MoO3: An in situ Raman spectroscopy study. *J. Phys. Chem.* **1994**, *98*, 11269−11275.
(32) Zhou, D.; Pang, L.-X.; Wang, H.; Guo, J.; Yao, X.; Randall, C. A. Phase transition, Raman spectra, infrared spectra, band gap and microwave dielectric properties of low temperature firing $(Na_{0.5x}Bi_{1-0.5x})(Mo_xV_{1-x})O_4$ solid solution ceramics with scheelite structures. *J. Mater. Chem.* **2011**, *21*, 18412−18420.
(33) Hanai, T. Theory of the dielectric dispersion due to the interfacial polarization and its application to emulsions. *Kolloid Z.* **1960**, *171*, 23−31.
(34) Gu, Y.-j.; Lei, L.-w.; Huang, J.-l.; Yang, X.-h.; Li, Q.; Li, L.-h.; Li, X.-l.; Kim, B.-h. A novel low-fired, temperature-stable, and low-cost (1-x)$BaCu(B_2O_5)$-xTiO_2 microwave dielectric ceramic. *J. Eur. Ceram. Soc.* **2019**, *39*, 1137−1141.
(35) Shannon, R. D. Dielectric polarizabilities of ions in oxides and fluorides. *J. Appl. Phys.* **1993**, *73*, 348−366.
(36) Huang, C.-L.; Weng, M.-H. Improved high Q value of $MgTiO_3$−$CaTiO_3$ microwave dielectric ceramics at low sintering temperature Mater. *Res. Bull.* **2001**, *36*, 2741−2750.
(37) Zurmühlen, R.; Petzelt, J.; Kamba, S.; Kozlov, G.; Volkov, A.; Gorshunov, B.; Dube, D.; Tagantsev, A.; Setter, N. Dielectric spectroscopy of $Ba(B_{1/2}'B_{1/2}')O_3$ complex perovskite ceramics: Correlations between ionic parameters and microwave dielectric properties. II. Studies below the phonon eigenfrequencies (102−1012 Hz). *J. Appl. Phys.* **1995**, *77*, 5351−5364.
(38) Lv, Y.; Zuo, R.; Cheng, Y.; Zhang, C. Low-Temperature Sinterable (1-x)$Ba_3(VO_4)_{2-x}$ $LiMg_{0.9}Zn_{0.1}PO_4$ Microwave Dielectric Ceramics. *J. Am. Ceram. Soc.* **2013**, *96*, 3862−3867.
(39) Petosa, A.; Ittipiboon, A. Dielectric resonator antennas: A historical review and the current state of the art. *IEEE Antennas Propag. Mag* **2010**, *52*, 91−116.
(40) Leung, K. W.; Lim, E. H.; Fang, X. S. Dielectric resonator antennas: From the basic to the aesthetic. *Proc. IEEE* **2012**, *100*, 2181−2193.
(41) Bi, K.; Wang, X.; Hao, Y.; Lei, M.; Dong, G.; Zhou, J. Wideband slot-coupled dielectric resonator-based filter. *J. Alloys Compd.* **2019**, *785*, 1264−1269.
(42) Pei, C.; Li, Y.; Tan, J.; Yao, G.; Jia, Y.; Liu, W.; Liu, P.; Zhang, H. Temperature stable (1-x)$NaCa_4V_5O_{17}$-xBaV_2O_6 microwave dielectric ceramics for ULTCC applications. *Ceram. Int.* **2020**, *46*, 27579−27583.
(43) Deng, Y.; Yao, P.; Li, B. A novel ultra-low temperature sintered Li_2CO_3 doped $Ba_3V_2O_8$ microwave ceramics. *Mater. Lett.* **2021**, *285*, 129125.
(44) Zhang, G.; Guo, J.; Yuan, X.; Wang, H. Ultra-low temperature sintering and microwave dielectric properties of a novel temperature stable $Na_2Mo_2O_7$-$Na_{0.5}Bi_{0.5}MoO_4$ ceramic. *J. Eur. Ceram. Soc.* **2018**, *38*, 813−816.
(45) Wang, S.-F.; Wang, Y.-R.; Hsu, Y.-F.; Tsai, J.-S. Densification, microstructure and microwave dielectric properties of ultra-low fire $BaTe_4O_9$-$TiTe_3O_8$ ceramic composites. *J. Eur. Ceram. Soc.* **2010**, *30*, 1737−1741.
(46) Jiao, X.; Zhong, C.; Zhang, S.; Liu, X.; Li, B. Microwave dielectric properties of BaO-TiO_2-TeO_2 ternary system. *J. Mater. Sci.* **2010**, *45*, 3331−3335.

https://doi.org/10.1021/acsaelm.1c00193
ACS Appl. Electron. Mater. 2021, 3, 2286−2296